Current Advances in Characterization of Nano-porous Materials: Pore Size Distribution and Surface Area

Kaihang Shi, Erik E. Santiso, and Keith E. Gubbins

Abstract Methods for characterizing the most important textural properties of porous materials, particularly pore size distribution (PSD) and specific surface area (SSA), using theoretical models to analyze standard experimental physisorption isotherms are reviewed. For PSD analysis, we explain the basics of the classical methods, including those based on the Kelvin equation and adsorption potential theory, as well the modern molecular methods based on the density functional theory (DFT) and molecular simulation. For SSA analysis, the discussion is focused on kinetic theory, and primarily on the application of the Brunauer-Emmett-Teller (BET) method for characterization of microporous materials. Current advances and extensions of model-based methods are discussed, including those related to machine learning techniques. We reflect on the limitations of the current state-of-the-art methods and point out some possible directions for future studies.

1 Introduction

The demand for accurate and fast characterization of porous materials has increased dramatically in recent years, due to the wide application of these materials to solve engineering and global environmental problems (for example, design of supercapacitors [1], hydrogen storage [2], and carbon capture [3]). The adsorption capacity [4, 5], phase equilibrium [6–8], and transport [9] of confined phases in porous materials are directly linked to their structure properties, such as specific surface area (SSA) and pore size distribution (PSD). Knowledge and control of the PSD and surface area of porous materials is of utmost importance in many applications, including medical and dental implants [10, 11], filtration [12, 13], catalysis [14–17], next-generation

K. Shi · E. E. Santiso · K. E. Gubbins
Department of Chemical and Biomolecular Engineering, North Carolina State University, Raleigh, NC 27695, USA

K. Shi (✉)
Department of Chemical and Biological Engineering, Northwestern University, Evanston, IL 60208, USA
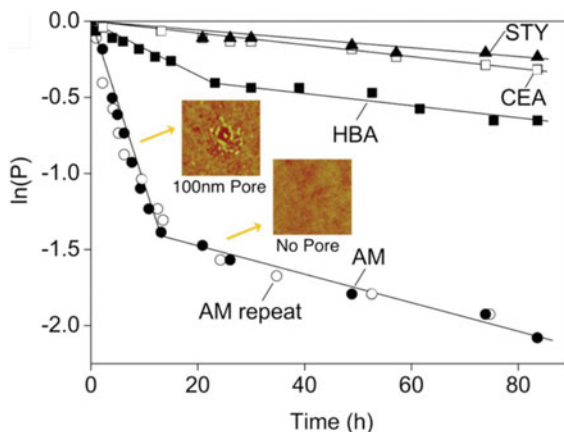e-mail: kshi@northwestern.edu

Fig. 1 Crystallization of aspirin on porous materials with different pore size distributions. $P(t)$ is the probability of no crystal forming at time (t). The pore sizes have a dramatic effect on the crystallization rate. Reprinted with permission from Ref. [25]. Copyright (2011) American Chemical Society

high-pressure manufacturing [18–22], geological applications (including storage of gas, oil, and water in reservoirs [23]), crystallization control (see an example in Fig. 1) [24, 25], among others. For this reason, the development of accurate, high-throughput techniques to determine PSD and SSA can have an impact in many different fields.

There is a long history of the development of both experimental and theoretical methods to obtain the textural properties of porous materials. Experimental methods for measuring the PSD include small-angle X-ray (SAXS) and neutron scattering (SANS), gas adsorption, mercury porosimetry, microscopy, and X-ray microtomography, among many others [26–28]. The experimental measurement of the SSA is often limited to the gas sorption method. Physisorption experiments are the most used techniques to understand the thermodynamic state of confined phases and the structure of porous materials. Physisorption has the advantage of being a convenient, non-destructive, and reversible method. Hybrid methods, combining physisorption experiments and theoretical models based on classical thermodynamics and statistical mechanics [29, 30], are able to extract much critical structural information of the porous materials, including the PSD and SSA, and they are performed as a routine analysis nowadays.

This book chapter focuses primarily on theory- and simulation-based hybrid approaches for the PSD and SSA characterization of porous materials, including some of the recent advances and extensions of the traditional approaches. The chapter is organized as follows: Sect. 2 describes methods for the determination of the PSD, including classical methods based on the Kelvin equation and the adsorption potential theory, as well as more modern methods based on the classical density functional theory (DFT) and grand canonical Monte Carlo (GCMC) simulation. Section 3 discusses methods to determine the SSA, including the widely used Brunauer-Emmett-Teller (BET) method, and discusses newer extensions of the BET method as well as modern approaches based on machine learning techniques. Finally, Sect. 4 provides some concluding remarks and outlines some possible future developments.

2 Pore Size Distribution

2.1 Classical Methods

Mesopore Analysis The adsorption behavior in mesopores (2–50 nm) depends not only on the solid-fluid interactions, but also on the fluid-fluid interactions, leading to the occurrence of pore condensation and multiplayer adsorption. Before the advent of statistical mechanical methods, mesopore size characterization generally made use of the correlation between the pore condensation pressure and the pore size, established by the Kelvin equation [31]. The Kelvin equation relates the shift of pore condensation pressure, P, relative to the bulk coexistence pressure, P_0, to the macroscopic properties:

$$\ln \frac{P}{P_0} = -\frac{2\gamma \bar{V}}{r RT} \tag{1}$$

where P is the actual vapor pressure (i.e., the pore condensation pressure, $P < P_0$), γ is the liquid/vapor surface tension, $\bar{V}$ is the molar volume of the liquid, r is the radius of the droplet (or pore radius), R is the gas constant and T is the temperature. However, Eq. (1) does not consider the pre-adsorbed layers near the pore wall before the pore condensation happens. The original Kelvin equation was later modified to correct this problem [32]. In the modified Kelvin equation, the variable r in Eq. (1) is replaced by $(r_p - t_c)$, where r_p and t_c are the actual pore radius and the critical thickness of the adsorbed films at which pore condensation occurs. The modified Kelvin equation serves as the basis for many methods developed for pore size analysis, among which are included the Barrett-Joyner-Halenda (BJH) method [33], which is the most widely-used method for mesopore size analysis. The typical procedure to obtain a PSD profile is to build a work-table, including the columns of the following parameters: relative pressure, the corresponding Kelvin radius [r, from Eq. (1)] and the thickness of the pre-adsorbed layers (t_c, by Halsey equation [34, 35] for example), the pore radius (r_p) at each relative pressure, the mean value of Kelvin radius and pore radius ($\bar{r}_p$), and the change of pre-adsorbed film thickness and of liquid volume (converted from experimental volumetric gas physisorption data). The mean values and changes of quantities are calculated between two consecutive pressure conditions. The pore volume at a certain $\bar{r}_p$ can be calculated based on these quantities. An example calculation of the PSD based on the modified Kelvin equation is demonstrated in Ref. [27]. All methods that are based on the classical Kelvin equation make three main assumptions:

1. The porous material is composed of a collection of well-defined pores (cylindrical or slit-shaped), and the solid-fluid interactions are negligible for pore condensation in the inner core.
2. The thermodynamic properties of the confined phase (liquid-like) are the same as those of the corresponding bulk phase.

3. The thickness of the pre-adsorbed multi-layers can be estimated by the statistical thickness of layers on non-porous materials which share similar surface chemistry (i.e., similar BET *C* value, see Sect. 3.1) to the porous sample.

The first assumption sets the limitation that the method can only be applied to large mesopores and macropores (see Fig. 2), and caution should always be exercised when applying this method to calculate the PSD of materials having small and connected pores. Gelb and Gubbins [36] showed that the BJH method yields a qualitatively similar PSD profile compared to the exact geometric PSD in porous glasses with complex pore shape and connectivity, but the BJH method underestimates the pore size in a systematic way for small mesopores (~ 2 to 4 nm, consistent with the data presented in Fig. 2). The second assumption leads to deviations in small pores, where the confined fluid is structured layer-by-layer. In addition, the surface tension of the curved interface at the nanoscale is no longer a constant, as in the planar case. According to the Tolman equation [37], the surface tension of a droplet depends on the radius of the curvature [38]. The third assumption makes it easy to correlate the thickness of the layer with pressure, but the effect of adsorbent surface curvature on the adsorption amount (and thus on the thickness of the layer) has been omitted. The third assumption is also the basic approximation adopted by many other classical
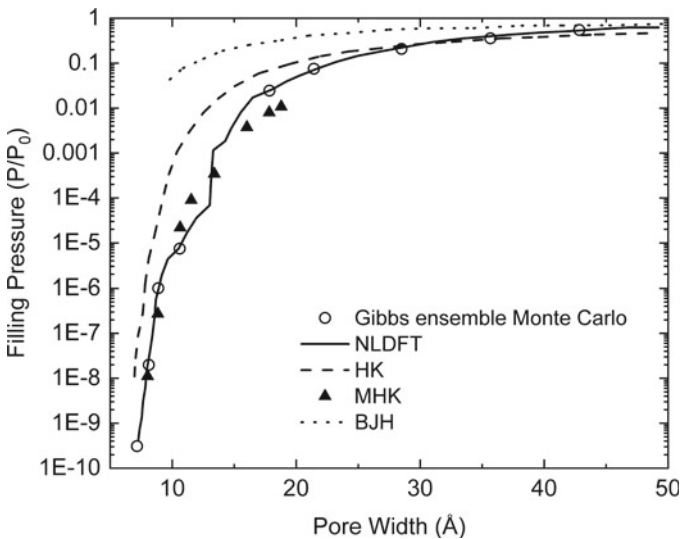
Fig. 2 Pore filling correlation predicted by Gibbs ensemble Monte Carlo (GEMC) simulation, non-local density functional theory (NLDFT), the original Horvath-Kawazoe (HK) method, modified Horvath-Kawazoe (MHK) method and the Barrett-Joyner-Halenda (BJH) method for nitrogen adsorption in carbon slit pores at 77 K. The HK method gives better agreement with the (exact) GEMC simulations than the modified Kelvin equation (BJH) in the micropore range, but performs more poorly in mesopores. The MHK method, using a more realistic 10-4-3 potential, gives better agreement with the NLDFT and GEMC simulations in micropores. The MHK data are from Ref. [48] and the rest are from Ref. [49, 50]

methods for the PSD analysis that involve predicting the layer thickness in pores. Nguyen and Do [39] showed that the PSDs calculated by the modified Kelvin equation in conjunction with an enhanced film thickness equation that depends on both pressure and pore size are comparable with those from the density functional theory.

Due to their theoretical simplicity and convenient implementation, methods based on the Kelvin equation (mainly the BJH method) are still widely used nowadays for analyzing the PSD of mesoporous materials. Efforts have been made to adapt the Kelvin equation to pores of finite length [40, 41], and to calibrate the performance of the BJH method for specific systems, such as for MCM-41 [42], CO_2 in activated carbon [43] and alumina samples having large and irregular slit-shaped mesopores (>10 nm) [44]. A general improvement of the BJH method has been made recently by introducing a correction term in the algorithm [45, 46]. The value of the correction term was chosen to fit the experimental isotherm data, and the PSD obtained by the proposed method is in favorable comparison with that from density functional theory [46]. The BJH method was originally developed for a single pore shape; it has been extended to analyze dual pore size distribution for coexistence of slit-shaped and cylindrical pores [47].

Micropore Analysis For micropores (< 2 nm), the Kelvin equation is no longer valid. Here we introduce several popular methods that have been widely used in the community to determine the PSD of microporous materials.

The micropore analysis (MP) method by Mikhail, Brunauer and Bodor [51] allows one to obtain the surface area, pore volume and PSD of the micropores from a single isotherm. The MP method can be considered as an extension of the *t*-method [52, 53], where the adsorbed liquid volume, V_{liq}, is plotted against the statistical thickness of the adsorbed film, t, which is determined from adsorbed films on nonporous materials having a similar BET C value, as a function of pressure. Once the $V_{liq} - t$ plot is made, the slope of the curve evaluated at a point between two thicknesses, t_i and t_{i+1}, is considered as the surface area of the pore that has not been filled:

$$S_{i+1} = \left. \frac{dV_{liq}}{dt} \right|_{r_h} \tag{2}$$

where the hydraulic radius is $r_h = \frac{(t_i + t_{i+1})}{2}$. The difference, $(S_i - S_{i+1})$, is the surface area for pores with hydraulic radii between t_i and t_{i+1} that has become filled. The pore volume corresponding to the hydraulic radius r_h can then be calculated by

$$V_i = (S_i - S_{i+1})r_h \tag{3}$$

The MP method is applicable to both slit-shaped and cylindrical pores, and the value $2r_h$ is the pore width for slit-shaped pores or the pore radius for cylindrical pores. Because the statistical thickness of the film gives the actual measure of the pore size in the MP method, it is not hard to imagine that the lack of statistical thickness data for certain adsorbents, and the approximation of the film thickness in pores to that on a non-porous material, will make the results from the MP method questionable.

The Dubinin-Radushkevich (DR) method provides another way to measure the micropore PSD, based on Polanyi's adsorption potential theory [54]. In Polanyi's theory, the adsorption potential A at a certain distance from the surface corresponds to the molar free energy to compress the vapor from pressure P, to the liquid state at the saturation pressure, P_0:

$$A = RT \ln \frac{P_0}{P} \tag{4}$$

The DR method postulates that the experimental micropore volume occupied by the condensed liquid, V_{liq}, follows a Gaussian distribution in terms of this adsorption potential,

$$V_{liq} = V_0 \exp\left[-\left(\frac{A}{\beta E_0}\right)^2\right] \tag{5}$$

where V_0 is the total micropore volume; β is the affinity coefficient defined as the characteristic adsorption energy of an adsorbate, E, to the reference value, E_0, where benzene was used as the reference adsorbate [55]. To extend the DR equation to heterogeneous surfaces, the exponent of the term, $\frac{A}{(\beta E_0)}$, in Eq. (5), is simply replaced by n, leading to the Dubinin-Astakhov (DA) equation [56]. The value of exponent n ranges from 2 to 6 in practice. The DR and DA formalisms have been compared in terms of adsorption potential distribution for pillared clays, zeolites and activated carbons [57]. The reference characteristic adsorption energy, E_0, has a one-to-one mapping to the pore size [55]. Therefore, for a real microporous material composed of a collection of different micropores, the PSD can be obtained by solving the integral equation [58]:

$$V_{liq} = \int f(E_0) \exp\left[-\left(\frac{A}{\beta E_0}\right)^2\right] dE_0 \tag{6}$$

where $f(E_0)$ is the PSD function in terms of the reference characteristic adsorption energy. It can be converted to the normal PSD by using the relation between the pore size and E_0 [55]. To solve Eq. (6), $f(E_0)$ is usually assumed to be the Gaussian distribution [58]. It has been shown that, without restricting $f(E_0)$ to a particular shape, the DR method is able to capture the bimodal PSD of chars [59]. The DR method in principle is not applicable to low pressures (Henry's law region). Sun [60] has modified the DR method to make it flexible enough to model the N_2 isotherm over a wide range of pressure.

Horvath and Kawazoe (HK) [61] introduced a simple PSD analysis that considers pore shape and molecular adsorbate-adsorbent interactions. They obtained a direct relation between the pore filling pressure and the physical pore width (defined as the distance between the nuclei of the two opposing pore surfaces for a slit-shaped pore) by equating the $(-A)$ in Eq. (4) to a uniform potential field. The uniform (unweighted)

potential field was obtained by spatially averaging the local 10-4 potential over the entire pore. Both adsorbate-adsorbent and adsorbate-adsorbate interactions were included in the potential field, although the adsorbate-adsorbate part was not handled correctly [48]. For nitrogen adsorbed in a microporous carbon material at 77.4 K, the pore filling correlation is given by [61]

$$\ln\left(\frac{P}{P_0}\right) = \frac{62.38}{H - 0.64}\left[\frac{1.895 \times 10^{-3}}{(H - 0.32)^3} - \frac{2.7087 \times 10^{-7}}{(H - 0.32)^9} - 0.05014\right] \quad (7)$$

where the physical pore width, H, is in units of nanometers. Thus, for a given physical pore width, a unique pore filling pressure, P, can be found (see Fig. 2). The HK method assumes the pore filling mechanism is discontinuous, that is, for each pressure, P, only pores that have physical pore width equal to or smaller than the corresponding physical pore width (calculated by Eq. (7), for example) are filled. The assumed discontinuous mechanism is a good approximation for small micropores but has been shown to be a source of error in the characterization of large micropores [62]. If we plot the experimental volume of adsorbed gas in its liquid state at a certain relative pressure versus the corresponding internal pore width, $w = H - \sigma_{ss}$, where σ_{ss} is the diameter of the adsorbent atom, we then have a $V_{liq} - w$ plot, i.e., a cumulative pore volume curve. The first-order gradient of the plot, $\frac{dV_{liq}}{dw}$, is the PSD. The HK method was originally developed for micropores having slit-shaped pores. It has been extended to cylindrical pores by Saito and Foley [63], and to spherical pores by Cheng and Yang [64]. Lastoskie and co-authors have modified the HK method by replacing the original unweighted potential field with a density-weighted integral [65] and by using a more realistic adsorbate-adsorbent potential (10-4-3 Steele potential [66]) and potential parameters [48]. It turned out that the latter modification, with the original unweighted scheme (here the adsorbate-adsorbate interaction was not included), yields a pore filling correlation in good agreement with the exact ones from the density functional theory and molecular simulation [48] (see Fig. 2 for MHK data). Although the HK method improves on the DR method by taking a realistic adsorbate-adsorbent potential and the pore geometry into account, it still makes the assumption that the thermodynamic properties of the confined phase are similar to those of the bulk phase, which is incorrect, as revealed by modern molecular methods based on statistical mechanics.

2.2 Modern Molecular Methods: Density Functional Theory and Molecular Simulations

The development of the statistical mechanical methods, including classical density functional theory (recently reviewed by Landers et al. [67]) and molecular simulations, has advanced the understanding of the fluids confined in pores, and leads to a universal approach that, in principle, enables the accurate characterization of

PSD over the complete pore range (micro-, meso- and macro-pores). The molecular methods have been considered superior to the classical methods, and they have been recommended as the standard ones for routine PSD analysis. They are available in commercial software for easy use by the experimentalists.

Classical Density Functional Theory (DFT) The principle behind DFT is that, for an open system, where molecules can freely exchange with a reservoir, the grand potential functional, Ω, can be written as a functional of local fluid density, $\rho(\mathbf{r})$, at position $\mathbf{r}$:

$$\Omega[\rho(\mathbf{r})] = F[\rho(\mathbf{r})] - \int d\mathbf{r}\,\rho(\mathbf{r})[\mu - V_{ext}(\mathbf{r})] \tag{8}$$

where F is the intrinsic Helmholtz free energy functional, μ is the chemical potential of adsorbate molecules, and $V_{ext}(\mathbf{r})$ is the spatially-varying external potential exerted by the pore walls. The integration is carried out over the entire system. We can obtain the equilibrium density profile $\rho_{eq}(\mathbf{r})$ by minimizing the functional derivative of the grand potential with respect to the fluid density profile, i.e.,

$$\left.\frac{\delta\Omega[\rho(\mathbf{r})]}{\delta\rho(\mathbf{r})}\right|_{\rho(\mathbf{r})=\rho_{eq}(\mathbf{r})} = 0 \tag{9}$$

When more than one minimum is present, the density profile that gives the lowest grand potential is the stable branch. Readers are referred to Hansen and McDonald [29] for detailed derivations of the DFT framework. Once the grand potential at equilibrium is known, other thermodynamic properties of the system are readily available, and the adsorbed amount in the pores (i.e., isotherm) can be calculated from the equilibrium density profile. The PSD is calculated by minimizing the following expression:

$$\left[n(P) - \int_{w_{\min}}^{w_{\max}} f(w)K(w, P)dw\right]^2 + \lambda\int_{w_{\min}}^{w_{\max}}\left[f''(w)\right]^2 dw \tag{10}$$

where $n(P)$ is the experimental specific adsorption or desorption isotherm at pressure P, the internal pore width is w, $f(w)$ is the pore size distribution function and $K(w, P)$ is the so-called kernel function which is the isotherm, predicted from either DFT or GCMC simulation at a specific pore size w. The integration in Eq. (10) is from the minimum pore width to the maximum pore width. Simply minimizing the first term in Eq. (10) for $f(w)$, however, is an ill-posed inverse problem, and a regularization term (second term in Eq. (10)) should be added, where λ is the regularization parameter. A stable numerical method for solving for $f(w)$ is available in the SAIEUS program [68, 69]. Seaton, Walton and Quirke [70] were the first to apply DFT to predict the PSD. Their method is based on the local version of DFT, which assumes that the specific free energy at a point $\mathbf{r}$ depends only on the local

density at that point, and so neglects effects of strong density gradients near the pore walls. Nevertheless, the local DFT provides significant improvement over the classical methods for PSD in both the mesopore and micropore range. However, it fails to reproduce the strong oscillations characteristic of the fluid density profile at a solid-fluid interface for small pores. Lastoskie et al. [50], and independently Olivier et al. [71], applied the non-local DFT (NLDFT) to the PSD analysis. Compared to the local version, the non-local version evaluates the excess Helmholtz free energy in the hard sphere term using a non-local density approximation [72, 73], that accounted for strong oscillations in the density profile near the pore walls. The NLDFT leads to quantitatively accurate fluid structure in nanopores compared to the local DFT, as has been confirmed by molecular simulations [74]. The consistency and validity of the NLDFT has further been confirmed by comparing the calculated PSD to experimental X-ray diffraction (XRD) measurements for porous materials with well-defined pore geometry [75, 76] (see Fig. 3). The PSD calculation using NLDFT generally makes the following main assumptions:

1. The pore wall is homogeneous and smooth [50, 77, 78]. For example, the 10-4-3 Steele potential derived from a homogeneous graphite surfaces is usually adopted for modeling a carbon slit-shaped pore [50].
2. Pores in the material have a single geometry and single-level surface heterogeneity.
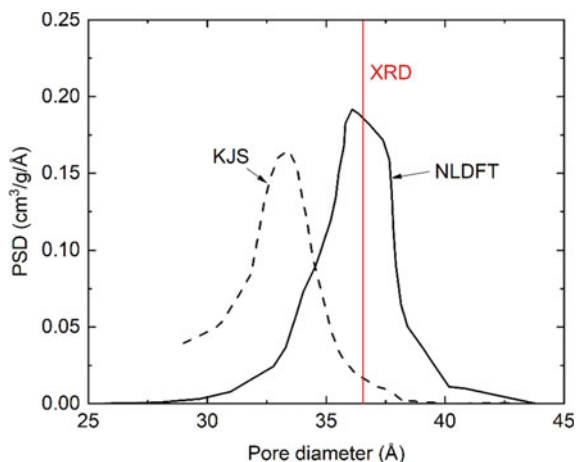
Fig. 3 Pore size distribution of MCM-41 sample AM-1 by Kruk-Jaroniec-Sayari (KJS) [42] method and NLDFT methods. KJS is a modified method based on the BJH method, and it was calibrated for MCM-41 materials. KJS method was found to be quite successful for MCM-41 materials in the pore size range of 2–6.5 nm, but for sample AM-1 here, it underpredicts the pore size by about 3 Å. The calculated PSD by the NLDFT method is in perfect agreement with the pore size from the XRD measurement. Adapted with permission from Ref. [76]. Copyright (2000) American Chemical Society

3. The pore size information can be fully extracted from a single-component adsorption or desorption isotherm.

It has been known for a long time that the first assumption leads to two artifacts: a typical S-shaped deviation from the experimental isotherm, due to layering transitions on the (assumed in the model) smooth surface, and a minimum in the PSD plot at a pore width of about 10 Å (see Fig. 4). In fact, nearly all real surfaces exhibit some degree of defects through geometric curvature, heteroatoms in the surface structure and chemical groups attached to the surface. Efforts have been devoted to eliminating
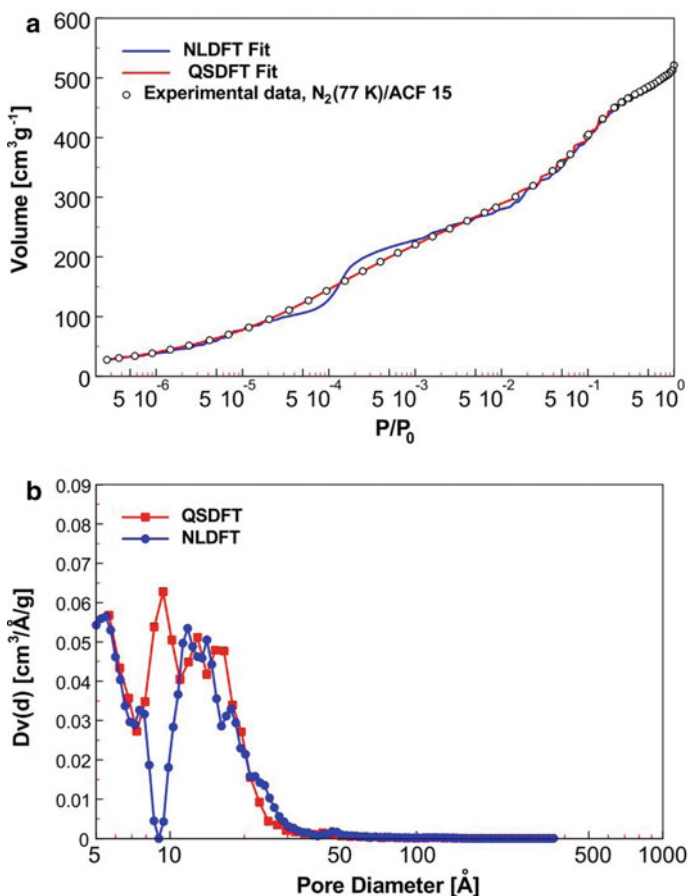

Fig. 4 Comparison of the NLDFT and QSDFT methods for nitrogen adsorption for activated carbon fiber ACF-15. **a** Experimental adsorption isotherm in comparison with the fitted isotherm by NLDFT and QSDFT methods. **b** PSD calculated by the NLDFT and QSDFT methods. The NLDFT method produces artifacts of a S-shaped isotherm and a minimum in the PSD plot at a pore width of about 10 Å. These two artifacts can be attributed to the homogeneous surface model used in the NLDFT method. QSDFT eliminates these two artifacts and presents a better fit to the experimental isotherm data. Adapted from Ref. [82], Copyright (2009), with permission from Elsevier

these two artifacts by introducing heterogeneities to the pore wall potential in the DFT framework. Examples are the introduction of an external potential accounting for variable wall thickness [79], variable surface density [80–82], incorporating pore edge effects [83, 84], and also models that incorporate a periodic function to the fluid-wall potential in a direction parallel to the pore surface [85–89]. Among these modifications, two notable versions are quenched solid density functional theory (QSDFT) and 2D-NLDFT. In QSDFT [81, 82], the geometrically heterogeneous pore wall is represented explicitly by a one-dimensional density profile of carbon atoms controlled by a single roughness parameter, while in 2D-NLDFT, by introducing periodic functions into the pore wall potential, both energetic and geometric heterogeneities of the pore wall have been accounted for either in a separate [85] or combined way [90]. Both methods eliminate the two artifacts of the traditional NLDFT method for activated carbon materials [82, 85] (see Fig. 4 for an example of QSDFT). When characterizing the same carbon materials, the QSDFT and 2D-NLDFT methods give similar PSD results [91]. This might be because both methods adjust the potential parameters for the carbon pore model by fitting the theoretical adsorption isotherm to the experimental data of the reference Cabot BP-280 [92]. For silica adsorbents, QSDFT calculates the parameters from the XRD measurement [93], while 2D-NLDFT fits potential parameters to the data of reference silica LiChrospher-Si-1000 [88]. It would be good to test both methods on the same silica materials and see if they give consistent results. In addition to modifying the pore wall model in the theory, Kupgan et al. [94] showed that, by tuning the regularization parameter, λ, in Eq. (10), the performance of NLDFT methods can also be improved for calculating the PSD of amorphous microporous materials. They proposed a smooth-shift method to obtain the regularization parameter in comparison to the conventional L-curve method [95]. The smooth-shifted PSD agrees well with the exact geometric PSD from molecular simulation. It is not clear, however, if the smooth-shifted method can eliminate the artifact of S-shaped adsorption isotherm from NLDFT.

The second assumption in NLDFT (single pore geometry and single-level surface heterogeneity) is not bad for a general PSD analysis. Allowing for the variation of the pore geometry and surface heterogeneity, however, adds more flexibility and reality to the theoretical model, leading to a better fitting to the experimental isotherm and better representation of the materials. Thommes et al. [96] developed a set of hybrid NLDFT kernels allowing for different pore geometries for hierarchically structured, micro-mesoporous silica materials. The hybrid kernels use a cylindrical pore model for micropores and small mesopores, and a spherical pore model for large mesopores where hysteresis occurs. The authors found that the hybrid approach is able to capture the full PSD in the complete micro- and meso-pore range, and the calculated PSD agreed with the results from independent SANS/SAXS measurement [96]. Gor et al. [97] were able to construct four different sets of hybrid kernels that use different pore geometry within different ranges of pore size, and these hybrid kernels have been successfully applied to characterize the micro-mesoporous carbons [97, 98]. Attempts to construct hybrid kernels allowing for different levels of surface heterogeneity have only been made recently. Lucena et al. [99] proposed a set of

hybrid kernels composed of simulated isotherms on surfaces having different levels of etching [100], covering from a homogeneous surface to a highly heterogenous surface. They have shown that employing the hybrid kernels for the PSD calculations reveals new structural details of the carbon porous materials (see Fig. 5). However, the use of the hybrid kernels requires a better understanding of the materials a priori, and so far no rational strategy has been proposed for choosing a suitable collection of kernels for the PSD calculations.

The third assumption (PSD can be fully extracted from a single-component isotherm) is the safest one and has been validated by comparing the calculated PSD with independent experimental measurements [67, 88, 96]. Although the pure adsorption/desorption kernels of N_2 at 77 K or Ar at 87 K are dominant in standard PSD calculations, it becomes problematic when analyzing fine micropores where the diffusion of N_2 is very slow [101], making the experimental measurement of equilibrium adsorption difficult to achieve. Recently, a dual gas analysis of PSD with the 2D-NLDFT method was proposed, where the adsorption data of N_2 & CO_2 [102, 103] or O_2 & H_2 (for minimal interaction of gas quadrupole moment with surface
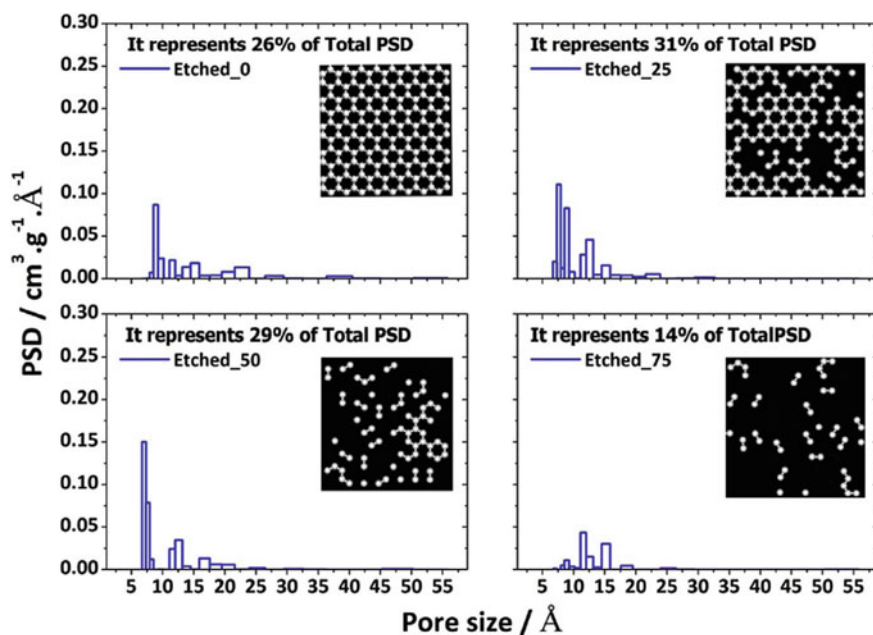
Fig. 5 Pore size distribution (PSD) by the hybrid kernels representing different levels of surface heterogeneity for PC58 sample. 26% of the total pore volume belong to pores having homogeneous surfaces, 31% of the total pore volume belong to pores having surfaces of 25% etching level, 29% of the total pore volume belong to pores having surfaces of 50% etching level, and 14% of the total pore volume belong to pores having surfaces of 75% etching level. Using the hybrid kernels reveal new information about the materials. Reprinted from Ref. [99]. Copyright (2017), with permission from Elsevier

polar sites) [104] were processed simultaneously to get a high-resolution PSD in full micro- and meso-pore range.

Monte Carlo Simulation GCMC simulation [105] is another method to get the kernels for PSD analysis. Unlike DFT, where the equations are numerically evaluated, the confined system in GCMC can be explicitly set up in a 3D simulation box with specified intermolecular force fields (see Fig. 6). The temperature, chemical potential and volume of the simulation box are pre-specified constants. During the simulation, the adsorbate molecules in the simulation box are in free exchange with a "ghost" bulk reservoir whose chemical potential is equal to the pre-set value (see Fig. 6). When enough exchanges (i.e., insertion or deletion move of molecules in the box) have been made, the simulation box is in chemical equilibrium with the "ghost" reservoir. Meanwhile, translational, and rotational (for non-spherical molecules) moves are also attempted randomly for adsorbate molecules in the simulation box to make sure the system eventually reaches the thermal equilibrium (assuming the structure of adsorbent is fixed). The Metropolis scheme is usually employed to determine if an attempted move should be accepted or declined. Once enough moves have been made for the simulation to reach equilibrium, the adsorption amount in the modeled

"Ghost" bulk reservoir

Particle exchange

Open-ended carbon slit pore
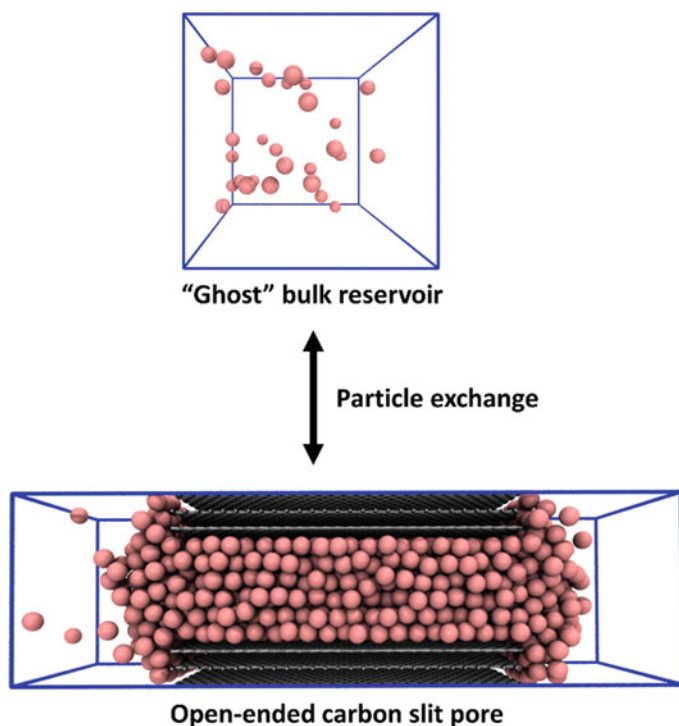
Fig. 6 Schematic of grand canonical Monte Carlo simulation. The argon molecules (pink particle) are in free exchange between the "ghost" bulk reservoir (top) and the simulation box (bottom). When chemical equilibrium is reached, the chemical potentials in both systems are equal

nanopore can then be directly calculated from the average over all equilibrium configurations of the molecules. In contrast to DFT-based methods, where some approximations are made (e.g., mean field approximation), the results from the GCMC simulation are considered to be exact for the model system (model for the intermolecular forces, pore geometry, etc.). In addition, the pore geometry and atomic surface structure can be modeled as realistically as desired in the GCMC simulation [99, 106–108]. However, consistency of the PSDs obtained from GCMC-based kernels and DFT-based kernels can be reached if suitable intermolecular parameters are chosen [109]. As of now, DFT-based kernels are still dominant over the GCMC-based kernels, mainly due to the fast execution of DFT calculations (minutes) compared to GCMC simulations (days). To explore the atomic details of the surface structure, or to access adsorption of complex molecules, this time expense must be paid, although some efforts to address this have been made on the DFT side recently by combining QSDFT and statistical associating fluid theory [110]. With increasing computational power and better understating of the surface structure at the microscopic scale, the GCMC method is expected to become more widely used in constructing the kernels for PSD determination.

3 Surface Area

3.1 Kinetic Theory

To characterize the surface area, kinetic theory remains the most successful and widely used method over the past century, thanks to its simplicity, satisfactory accuracy, and the clear physical meanings behind the concepts involved. The Langmuir equation and BET equation form the foundation of the adsorption kinetic theory for monolayer adsorption and multilayer adsorption, respectively.

Langmuir Equation In 1918, Langmuir [111] proposed the first quantitative description of monolayer adsorption (including chemisorption) by viewing adsorption onto the surface as a reversible chemical reaction. If only one type of surface site is available, the adsorption reaction can be written as:

$$A + S \rightleftarrows \text{AS}$$

where A is adsorbate, S is an unoccupied surface site, and AS is the surface site occupied by adsorbate through chemical forces. By equating the adsorption reaction rate to the desorption rate, the Langmuir equation can be recovered:

$$n = n_m \frac{KP}{1 + KP} \tag{11}$$

where n is the experimental specific adsorbed amount (e.g., in units of mol/g) at the partial pressure of the adsorbate, P; n_m is the monolayer saturation capacity, and K is the adsorption equilibrium constant. To obtain the surface area of the material, Eq. (11) is fitted to the experimental adsorption isotherm. The SSA, a_s, is calculated by

$$a_s = n_m N_A \sigma_m \tag{12}$$

where N_A is Avogadro's number and σ_m is the molecular cross-sectional area. The application of Langmuir's equation should, in principle, be limited to the monolayer adsorption on non-porous materials, but it is often applied to the general adsorption isotherm of Type I (see Fig. 7) which also represents adsorption behavior in microporous materials. Without a deep understanding of the pore topology and pore filling mechanism in microporous materials, a good fit of the Langmuir equation to the experimental isotherm should only be interpreted as the mathematical effectiveness

Fig. 7 International Union of Pure and Applied Chemistry (IUPAC) classification of physisorption isotherms. Reprinted with permission from Ref. [26]. Copyright (2015) IUPAC & De Gruyter
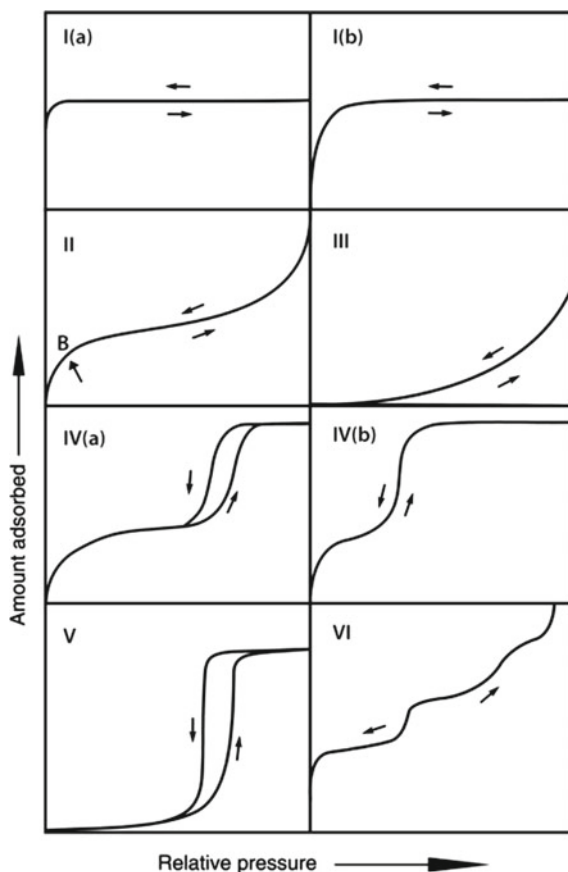
of the model, and the surface area obtained usually does not reflect the true surface area. The Langmuir equation assumes the surface is homogeneous. For adsorption on heterogeneous surfaces, several semi-empirical equations have been proposed based on the Langmuir equation and the Freundlich isotherm, such as the Sips equation [112] and the Toth equation [113]. There is no preference for one empirical model over the other, and the choice of a particular equation usually depends on their fitting quality to the experimental isotherm data of Type I shape.

Brunauer-Emmett-Teller (BET) Equation In reality, almost all monolayer adsorption on an open surface will be followed by the stacking of second, third and higher layers as the gas pressure is increased. In 1938, Brunauer, Emmett and Teller [114] extended the Langmuir formulation to a multilayer adsorption scenario, by considering the formation of higher layers on top of the first adsorbed layer as a dynamic process. The BET theory is based on the following assumptions:

1. The surface is atomically homogeneous, and adsorption occurs only on well-defined surface sites (i.e., one adsorbate molecule per surface site).
2. The pre-adsorbed molecules act as further well-defined adsorption sites for gas molecules to occupy, and the interactions between the adsorbate molecules in the same layer are ignored.
3. The heat of adsorption for the second, third and higher layers is the same as the heat of liquefaction of the adsorbing gas, but different from that for the first layer.
4. At the saturation pressure, P_0, the adsorption layer becomes infinitely thick (this serves as a boundary condition).

Following a similar argument as that of Langmuir, at equilibrium, the "formation" rate of a certain layer should be equal to the "destruction" rate of that layer. For example, when the first layer reaches the equilibrium, we have

$$R_1 + R_{-2} = R_{-1} + R_2 \qquad (13)$$

where R_1 is the rate of condensation onto the bare surface, R_{-2} is the rate of evaporation from the second layer, R_{-1} is the rate of evaporation from the first layer, and R_2 is the rate of condensation onto the second layer. The rate is directly related to the surface area covered by the layer. For example,

$$\begin{aligned} R_1 &= k_1 P \theta_0 \\ R_{-2} &= k_{-2} \theta_2 \end{aligned} \qquad (14)$$

where k_1 and k_{-2} are the rate constants, θ_0 and θ_2 are the empty surface area and the area covered by the second layer, respectively. Figure 8 presents a diagram for BET multilayer adsorption. By writing equations similar to Eq. (13) for all other adsorbed layers and applying the boundary condition (point 4 listed above), the BET equation can be eventually reached as [114]:

Fig. 8 BET model of multilayer adsorption. The total surface area is the sum of the empty area (θ_0), the area covered by the first adsorbed layer (θ_1), the area covered by the second adsorbed layer (θ_2), and so on
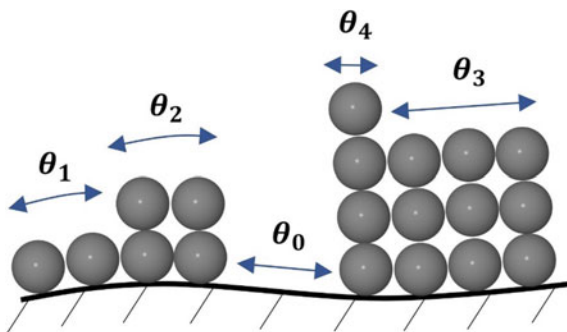
$$\frac{1}{n\left(\frac{P_0}{P}-1\right)} = \frac{C-1}{n_m C} \times \frac{P}{P_0} + \frac{1}{n_m C} \tag{15}$$

where C is the BET constant, which is directly related to the adsorbate-adsorbent interaction strength. Equation (15) can also be rigorously derived from statistical mechanics [115, 116]. By plotting experimental adsorption data as $\frac{P}{[n(P_0-P)]}$ versus relative pressure, $\frac{P}{P_0}$ ("the BET plot"), a linear correlation can usually be found as $\frac{P}{P_0}$ ranges from 0.05 to 0.3 for isotherms of Type II, IV and VI (see Fig. 7). By fitting such linear data with Eq. (15), the specific monolayer capacity, n_m, can then be determined, which leads to the estimation of the specific BET surface area of the materials [using Eq. (12)]. Because argon molecules do not have a quadrupole moment, and are less sensitive to the surface chemistry, IUPAC (2015) [26] recommends using argon at 87 K (its normal boiling point) as the standard adsorption condition for characterization.

## 3.2 Current Advances in Characterization of Microporous Materials by the BET Method and Beyond

BET Method Most of the porous materials that present excellent performance in real applications (such as gas storage and separation) contain micropores. Because of its restrictive assumptions, the Langmuir equation is rarely used in practice. Although the BET equation was also derived from several simplified assumptions (including the assumption that the adsorption is on open surfaces), scientists still found it convenient and useful for characterizing microporous materials. The most common issue associated with BET analysis of microporous materials is that multiple linear regions can be found in the BET plot for fitting, which leads to inconsistency of the calculations. To enhance the reproducibility, Rouquerol et al. [117] proposed four consistency criteria, which were later recommended by IUPAC (2015) [26], to locate a linear region objectively:

1. The BET C constant obtained from fitting should be positive to be meaningful.
2. The BET fitting range should be restricted to the region where the quantity $n(P_0 - P)$ continuously increases with $\frac{P}{P_0}$.
3. The $\frac{P}{P_0}$ value in the experimental isotherm that corresponds to the monolayer capacity, n_m, should be in the selected fitting range.
4. The relative pressure calculated from the fitted BET equation [Eq. (15)] by setting $n = n_m$ should not differ from the experimental one (from criterion 3) by more than 20% [118].

Following the above consistency criteria, we can obtain the SSA that belongs to the micropores, a_{micro}, by

$$a_{micro} = a_{BET} - a_{ext} \tag{16}$$

where a_{BET} is the specific BET surface area; a_{ext} is the specific surface area contributed from external (i.e., non-microporous) surfaces, which can be calculated with the help of the t-method [52, 53] or the α_s-method [119]. Walton and Snurr [120] have shown that these consistency criteria lead to a better BET surface area characterization for six microporous metal organic frameworks (MOFs), with the calculated values being in good agreement with the geometric (accessible) surface area calculated directly from the MOF atomic structure. It has recently been confirmed that, based on the calculation of true monolayer surface area [121] from molecular data for over 200 MOFs, the BET theory along with these consistency criteria can, in general, produce reasonable surface areas for MOFs with a high volumetric percentage of small micropores (pore diameter < 10 Å and surface area < 1500 m^2/g) [122]. Although the consistency criteria help standardize the BET analysis, they do not always lead to the correct identification of the pressure range where monolayer formation occurs, especially for porous materials having a combination of large micropores (10 Å < pore diameter < 20 Å) and mesopores (pore diameter > 20 Å) [121, 122]. The adsorption isotherm of these porous materials shows a characteristic step-wise pattern, and the consistency criteria tend to choose the pressure range where micropore pore filling occurs, thus usually overestimating the surface area. To locate the correct region for monolayer formation, Sinha et al. [122] proposed to use the excess sorption work (ESW) method together with the BET equation (termed as BET+ESW method). The ESW method [123, 124] was designed to determine the monolayer capacity directly from the adsorption isotherm without referring to any adsorption model. By plotting the excess sorption work, $\phi = nRT \ln\left(\frac{P}{P_0}\right)$, versus the adsorption loading, n, the monolayer capacity is expected to be the loading at the first local minimum in the $(\phi - n)$ plot (i.e., ESW plot). Although the ESW method alone usually underestimates the actual surface area [122], it can predict a rough pressure value that corresponds to the monolayer formation. Therefore, in addition to the first and second consistency criteria listed above, a new third criterion was suggested that the BET linear region should be chosen such that it includes the pressure that corresponds to the first minimum in the ESW plot (see Fig. 9 for an
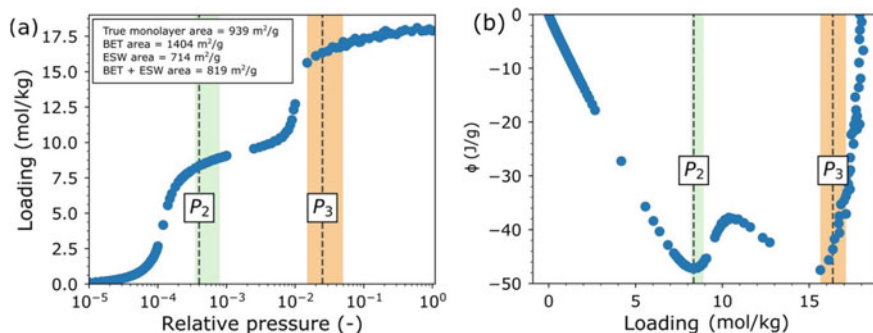
Fig. 9 The BET+ESW method for estimating the surface area of a carbon nanotube with diameter of 16.9 Å. **a** Adsorption isotherm. **b** The ESW plot. The ochre region is the BET fitting range determined from original four consistency criteria, and the green region is the new BET range determined by BET+ESW method. The first local minimum in the ESW plot corresponds to the pressure P_2, and the new BET fitting range is chosen to include this pressure. The BET+ESW method gives a specific surface area of 819 m²/g, that is closer to the true surface area (939 m²/g) than other methods. Reprinted with permission from Ref. [122]. Copyright (2019) American Chemical Society

example). The BET+ESW method has been shown to improve the surface area estimation for porous materials that contain large micropores and mesopores, however, it fails when no clear minimum is present in the ESW plot. In some cases, the micropores are so small that the first minimum in the ESW plot corresponds to micropore filling that finishes before the monolayer formation. The result is that the BET+ESW method tends to suggest the wrong BET fitting range, while the original consistency criteria work better. Therefore, the BET+ESW method cannot guarantee the correct estimation of the true monolayer surface area, but can serve as a supplement to the standard BET analysis to prevent overestimation [122]. It should be noticed that, when monolayer formation and pore filling become indistinguishable, even if all consistency criteria are satisfied, the BET related methods are unable to predict the correct surface area. In such cases, the BET plot only exhibits one linear region where the monolayer formation and pore filling occurs simultaneously, and the monolayer capacity determined from the BET method now also includes the non-monolayer amount, thus overestimating the surface area. It has been shown that this kind of pore indistinguishability happens for slit-shaped pores that can accommodate three adsorption layers (pore size of about 10 Å) [125]. Theories that are beyond the BET method, or additional adsorption data, are required to effectively separate the monolayer capacity from the pore filling.

According to Eq. (12), in addition to the monolayer capacity, the other source of error in the BET method is the molecular cross-sectional area, σ_m. As shown by Brunauer and coworkers in their 1937 [126] and 1938 [114] papers, and somewhat later in the monograph by Brunauer [127], the close packing of the adsorbate molecules on the substrate surface results in a surface area per molecule that is 7–19% smaller than expected, based on the density of the bulk liquid for these same gases. In

principle, the molecular cross-sectional area should be correlated to the packing state of the monolayer, and they should vary with the adsorbent, adsorption temperature and the choice of reference system (usually nitrogen is used as reference [128–130]). However, in practice, people usually treat the molecular cross-sectional area as a constant. Based on the liquid packing of the layer, values of the molecular cross-sectional area of 16.2 $Å^2$ and 13.8 $Å^2$ have become conventional for nitrogen and argon adsorption, respectively [131]. The practical reasons for choosing a constant σ_m might be obvious: it is convenient; and for adsorption in microporous materials, the error in obtaining the correct monolayer capacity is usually larger than that of the choice of the molecular cross-sectional area, and sometimes the errors in n_m and σ_m may compensate each other. Nevertheless, we should still keep in mind that the choice of molecular cross-sectional area also matters in surface area calculations.

Beyond the BET Equation Since the original work of Langmuir [111] and Brunauer et al. [114], no major breakthrough has been made in the field of adsorption theory. This is partly because the BET theory is convenient and simple, and it has already been proved suitable for characterizing both porous and non-porous materials [132]. Most of the real porous materials contain hierarchical pores and pore connectivity, making the development of a general adsorption theory very difficult. Recently, advances in machine learning (ML) techniques [133] have opened up a new route to estimating the SSA from experimental data; in principle, such data do not necessarily have to be the physisorption isotherms. Figure 10 shows a general supervised ML workflow. In the case of predicting the surface area, a set of *features* that can describe the materials is first designed. Features need to be experimentally measurable, representative, and informative. A set of training data are then prepared, and they include representative materials, whose surface area (*label*) has been accurately pre-calculated from either simulation or direct measurement. The ML model (e.g., artificial neural networks
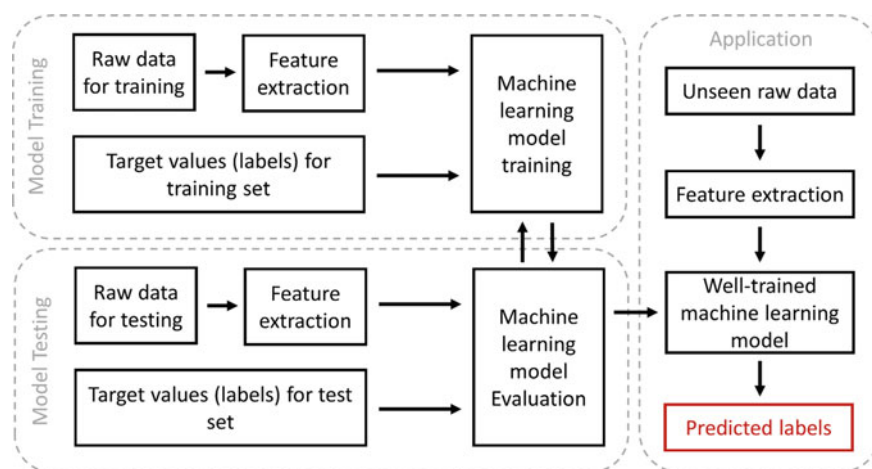
Fig. 10 A general supervised machine learning workflow

[133]) is subsequently trained using the training set with *features* as input and *labels* as the output target. If the ML model is properly trained without overfitting or under-fitting, it can then be used to predict the surface area of other unseen materials by simply feeding the *features* of those materials into the well-trained ML model. The advantage of the ML method is clear: it enables prediction of the surface area through this large-scale regression algorithm without knowing the underlying physics of adsorption. This, however, can also be considered a disadvantage, as most ML models operate as "black boxes" that do not provide physical insight on the process. Attempts to use ML methods for surface area predictions have only been made very recently. Datar et al. [134] considered the mean loading in various pressure regions of the isotherm as the *feature*. They trained the least absolute shrinkage and selec-tion operator (LASSO) model [135], using a training set of more than 300 MOFs with diverse structures and pre-calculated true monolayer surface area. They have shown that the ML model outperforms the BET method in the entire surface area region (see Fig. 11). In addition to extracting the materials' structure information from the normal adsorption isotherm, the micro-computed tomography (micro-CT) X-ray images can also serve as the input data [136]. With the power of convolutional neural networks [137], Alqahtani et al. [136] were able to predict the porosity, SSA, and average pore size for each input image. Although the physisorption isotherm still remains one of the most accessible sources of data for many laboratories, the ML methods open up a lot of possibilities to extract information from various sources of data, thus providing a more flexible, general and fast way to predict the properties of porous materials.
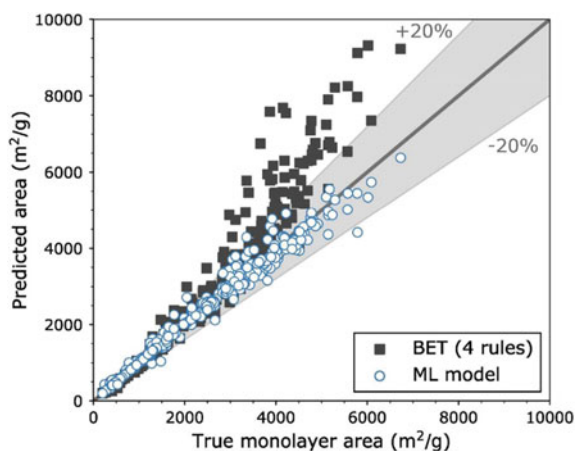
Fig. 11 Comparison between the predicted surface area by the BET method (satisfying the four consistency criteria of Rouquerol et al. [117]) and by the machine learning (ML) model. The ML model offers overall excellent prediction over a wide range of areas in agreement with the true surface area from molecular simulations. Adapted with permission from Ref. [134]. Copyright (2020) American Chemical Society

4   Concluding Remarks and Future Perspective

In this chapter, we have reviewed the characterization of the PSD and the SSA of porous materials by model-based hybrid methods. These methods extract the structural information of the materials from the experimental physisorption isotherms.

For PSD analysis, we have first introduced the classical methods, including those based on the Kelvin equation for mesopore analysis, and those for micropore analysis (MP method, DR/DA method, and HK method). The basics of the modern molecular methods (DFT and GCMC simulation) based on statistical mechanics are also explained. The modern molecular methods are superior to the classical methods in the complete pore size range, and they are recommended for routine PSD analysis.

For SSA analysis, we have focused on the kinetic theory (Langmuir and BET equations), and the application of the BET method for characterization of microporous materials. With the four consistency criteria proposed by Rouquerol et al. [117] and the recently proposed BET+ESW method, the BET equation is able to determine the surface area of the porous materials having micro- and mesopores. The accuracy of the BET surface area, however, should be cautiously examined with the understanding of the pore structure (e.g., PSD, pore geometry).

Some current challenges for the PSD and surface area analysis, and possible future directions are summarized as follows:

1. The current state-of-the-art methods for rapid characterization of the PSD are those based on statistical mechanics, namely DFT or GCMC simulations. However, more experimental evidence is needed to refine the effective solid-fluid potentials (in DFT methods) [138–141] and the pore models (in GCMC simulations). Only a few pre-calculated kernels for specific materials and pore geometries (such as a slit-shaped carbon pore) are typically available in the commercial software, yet those kernels are often used to characterize novel materials with varied chemical compositions and pore shapes (e.g., MOFs), which is in principle incorrect, and it often results in misleading PSDs even if the fit to the experimental isotherm is good. Resolving this discrepancy would require a rational strategy to combine a set of kernels representing the surface chemistry and pore geometry of the materials, with algorithms for fast generation of the custom kernels.

2. Due to the simplified assumptions, it is impossible to apply the BET equation to any materials with hierarchical pore structures. Especially, the BET equation will fail when monolayer formation and pore filling occur simultaneously. Recent developments in ML-based methods provide a new route for fast characterization of surface area. We anticipate that new, general ML models with the ability to predict the surface area of materials over the entire range of pore sizes will be developed in the near future. This involves the development of advanced ML algorithms and design of suitable *feature* set. It should be noted that, however, the ML model is usually trained with the simulation data (i.e., simulated isotherm and geometric surface area). When applying those simulation-data-trained models to

predict surface area in practice, the fidelity of materials' models in simulations should be carefully checked, so that the established correlation between *features* and *labels* can be safely translated from simulated world to the real world.

3. Some materials are not rigid and have a flexible skeleton. The deformation of the structure during the adsorption process [142] can affect the surface area and PSD analysis of the material. Future characterization tools should consider this effect to provide a more complete description of porous materials.

References

1. Kondrat, S., Pérez, C.R., Presser, V., Gogotsi, Y., Kornyshev, A.A.: Energy Environ. Sci. **5**, 6474 (2012)
2. Sdanghi, G., Canevesi, R.L.S., Celzard, A., Thommes, M., Fierro, V.: J. Carbon Res. **6**, 46 (2020)
3. Sumida, K., Rogow, D.L., Mason, J.A., McDonald, T.M., Bloch, E.D., Herm, Z.R., Bae, T.-H., Long, J.R.: Chem. Rev. **112**, 724 (2012)
4. Bobbitt, N.S., Chen, J., Snurr, R.Q.: J. Phys. Chem. C **120**, 27328 (2016)
5. Suresh Kumar, P., Korving, L., Keesman, K.J., van Loosdrecht, M.C.M., Witkamp, G.-J.: Chem. Eng. J. **358**, 160 (2019)
6. Gelb, L.D., Gubbins, K.E., Radhakrishnan, R., Sliwinska-Bartkowiak, M.: Rep. Prog. Phys. **62**, 1573 (1999)
7. Luo, S., Lutkenhaus, J.L., Nasrabadi, H.: Fluid Phase Equilib. **487**, 8 (2019)
8. Alba-Simionesco, C., Coasne, B., Dosseh, G., Dudziak, G., Gubbins, K.E., Radhakrishnan, R., Sliwinska-Bartkowiak, M.: J. Phys.: Condens. Matter **18**, R15 (2006)
9. Lian, C., Su, H., Li, C., Liu, H., Wu, J.: ACS Nano **13**, 8185 (2019)
10. Worthington, K.S., Wiley, L.A., Mullins, R.F., Tucker, B.A., Nuxoll, E.: J. Biomed. Mater. Res. Part B Appl. Biomater. **104**, 1602 (2016)
11. Li, G., Wang, L., Pan, W., Yang, F., Jiang, W., Wu, X., Kong, X., Dai, K., Hao, Y.: Sci. Rep. **6**, 34072 (2016)
12. Chang, J.S., Vigneswaran, S., Kandasamy, J.K., Tsai, L.J.: Sep. Sci. Technol. **43**, 1771 (2008)
13. Yang, H., Min, X., Xu, S., Bender, J., Wang, Y., Sustain, A.C.S.: Chem. Eng. **8**, 2531 (2020)
14. Santiso, E.E., George, A.M., Turner, C.H., Kostov, M.K., Gubbins, K.E., Buongiorno-Nardelli, M., Sliwinska-Bartkowiak, M.: Appl. Surf. Sci. **252**, 766 (2005)
15. Iwamoto, M., Tanaka, Y., Sawamura, N., Namba, S.: J. Am. Chem. Soc. **125**, 13032 (2003)
16. Santiso, E.E., Buongiorno Nardelli, M., Gubbins, K.E.: J. Chem. Phys. **128**, 034704 (2008)
17. Gubbins, K.E., Liu, Y.-C., Moore, J.D., Palmer, J.C.: Phys. Chem. Chem. Phys. **13**, 58 (2011)
18. Urita, K., Shiga, Y., Fujimori, T., Iiyama, T., Hattori, Y., Kanoh, H., Ohba, T., Tanaka, H., Yudasaka, M., Iijima, S., Moriguchi, I., Okino, F., Endo, M., Kaneko, K.: J. Am. Chem. Soc. **133**, 10344 (2011)
19. Fujimori, T., Morelos-Gómez, A., Zhu, Z., Muramatsu, H., Futamura, R., Urita, K., Terrones, M., Hayashi, T., Endo, M., Young Hong, S., Chul Choi, Y., Tománek, D., Kaneko, K.: Nat. Commun. **4**, 2162 (2013)

20. Vasu, K.S., Prestat, E., Abraham, J., Dix, J., Kashtiban, R.J., Beheshtian, J., Sloan, J., Carbone, P., Neek-Amal, M., Haigh, S.J., Geim, A.K., Nair, R.R.: Nat. Commun. **7**, 12168 (2016)
21. Gubbins, K.E., Gu, K., Huang, L., Long, Y., Mansell, J.M., Santiso, E.E., Shi, K., Śliwińska-Bartkowiak, M., Srivastava, D.: Engineering **4**, 311 (2018)
22. Srivastava, D., Turner, C.H., Santiso, E.E., Gubbins, K.E.: J. Phys. Chem. B **122**, 3604 (2018)
23. Anovitz, L.M., Cole, D.R.: Rev. Mineral. Geochem. **80**, 61 (2015)
24. Santiso, E.E.: Mol. Simul. **40**, 664 (2014)
25. Diao, Y., Myerson, A.S., Hatton, T.A., Trout, B.L.: Langmuir **27**, 5324 (2011)
26. Thommes, M., Kaneko, K., Neimark, A.V., Olivier, J.P., Rodriguez-Reinoso, F., Rouquerol, J., Sing, K.S.W.: Pure Appl. Chem. **87**, 1051 (2015)
27. Lowell, S., Shields, J.E., Thomas, M.A., Thommes, M.: Characterization of Porous Solids and Powders: Surface Area, Pore Size and Density. Springer, Netherlands, Dordrecht (2004)
28. Espinal, L.: Characterization of Materials. Wiley, Hoboken (2012)
29. Hansen, J.-P., McDonald, I.R.: Theory of Simple Liquids, 4th edn. Academic Press, Oxford (2013)
30. Allen, M.P., Tildesley, D.J.: Computer Simulation of Liquids, 2nd edn. Oxford University Press (2017)
31. Thomson, W.: Lon. Edinb. Dublin Philos. Mag. J. Sci. **42**, 448 (1871)
32. Cohan, L.H.: J. Am. Chem. Soc. **60**, 433 (1938)
33. Barrett, E.P., Joyner, L.G., Halenda, P.P.: J. Am. Chem. Soc. **73**, 373 (1951)
34. Halsey, G.: J. Chem. Phys. **16**, 931 (1948)
35. Dollimore, D., Heal, G.R.: J. Appl. Chem. **14**, 109 (1964)
36. Gelb, L.D., Gubbins, K.E.: Langmuir **15**, 305 (1999)
37. Tolman, R.C.: J. Chem. Phys. **17**, 333 (1949)
38. Santiso, E., Firoozabadi, A.: AIChE J. **52**, 311 (2006)
39. Nguyen, C., Do, D.D.: Langmuir **15**, 3608 (1999)
40. Malijevský, A., Parry, A.O., Pospíšil, M.: Phys. Rev. E **96**, 020801 (2017)
41. Malijevský, A., Parry, A.O.: Phys. Rev. Lett. **120**, 135701 (2018)
42. Kruk, M., Jaroniec, M., Sayari, A.: Langmuir **13**, 6267 (1997)
43. Yin, G., Liu, Q., Liu, Z., Wu, W.: Fuel Process. Technol. **174**, 118 (2018)
44. Huang, B., Bartholomew, C.H., Woodfield, B.F.: Microporous Mesoporous Mater. **184**, 112 (2014)
45. Villarroel Rocha, J., Barrera, D., Sapag, K.: Top. Catal. **54**, 121 (2011)
46. Villarroel-Rocha, J., Barrera, D., Sapag, K.: Microporous Mesoporous Mater. **200**, 68 (2014)
47. Liu, J., Li, P., Sun, Z., Lu, Z., Du, Z., Liang, H., Lu, D.: Fuel **210**, 446 (2017)
48. Dombrowski, R.J., Lastoskie, C.M., Hyduke, D.R.: Colloids Surf., A: Physicochem. Eng. Asp. **187–188**, 23 (2001)
49. Lastoskie, C.M., Quirke, N., Gubbins, K.E.: Stud. Surf. Sci. Catal., 745–775 (1997)
50. Lastoskie, C., Gubbins, K.E., Quirke, N.: J. Phys. Chem. **97**, 4786 (1993)
51. Mikhail, R.S., Brunauer, S., Bodor, E.: J. Colloid Interface Sci. **26**, 45 (1968)
52. Lippens, B.C., de Boer, J.H.: J. Catal. **4**, 319 (1965)
53. de Boer, J.H., Lippens, B.C., Linsen, B.G., Broekhoff, J.C.P., van den Heuvel, A., Osinga, T.J.: J. Colloid Interface Sci. **21**, 405 (1966)
54. Polanyi, M.: Verh. Dtsch. Phys. Ges. **16**, 1012 (1914)
55. Dubinin, M., Stoeckli, H.: J. Colloid Interface Sci. **75**, 34 (1980)
56. Dubinin, M.M., Astakhov, V.A.: Adv. Chem., 69–85 (1971)
57. Gil, A., Grange, P.: Colloids Surf., A Physicochem. Eng. Asp. **113**, 39 (1996)
58. Stoeckli, H.: J. Colloid Interface Sci. **59**, 184 (1977)
59. Pinto, M.L., Mestre, A.S., Carvalho, A.P., Pires, J.: Ind. Eng. Chem. Res. **49**, 4726 (2010)
60. Sun, J.: Carbon N. Y. **40**, 1051 (2002)
61. Horváth, G., Kawazoe, K.: J. Chem. Eng. Japan **16**, 470 (1983)
62. Valladares, D.L., Rodríguez Reinoso, F., Zgrablich, G.: Carbon N. Y. **36**, 1491 (1998)
63. Saito, A., Foley, H.C.: AIChE J. **37**, 429 (1991)
64. Cheng, L.S., Yang, R.T.: Chem. Eng. Sci. **49**, 2599 (1994)

65. Lastoskie, C.M.: Stud. Surf. Sci. Catal., 475–484 (2000)
66. Steele, W.A.: Surf. Sci. **36**, 317 (1973)
67. Landers, J., Gor, G.Y., Neimark, A.V.: Colloids Surf., A Physicochem. Eng. Asp. **437**, 3 (2013)
68. Jagiello, J.: Langmuir **10**, 2778 (1994)
69. Micromeritics, http://www.nldft.com/download/ (n.d.)
70. Seaton, N.A., Walton, J.P.R.B., Quirke, N.: Carbon N. Y. **27**, 853 (1989)
71. Olivier, J.P., Conklin, W.B., Szombathely, M. v.: Stud. Surf. Sci. Catal., 81–89 (1994)
72. Tarazona, P.: Phys. Rev. A **31**, 2672 (1985)
73. Tarazona, P., Marconi, U.M.B., Evans, R.: Mol. Phys. **60**, 573 (1987)
74. Lastoskie, C., Gubbins, K.E., Quirke, N.: Langmuir **9**, 2693 (1993)
75. Neimark, A.V., Ravikovitch, P.I., Grün, M., Schüth, F., Unger, K.K.: J. Colloid Interface Sci. **207**, 159 (1998)
76. Sonwane, C.G., Bhatia, S.K.: J. Phys. Chem. B **104**, 9099 (2000)
77. Ravikovitch, P.I., Haller, G.L., Neimark, A.V.: Adv. Colloid Interface Sci. **76–77**, 203 (1998)
78. Ravikovitch, P.I., Neimark, A.V.: Langmuir **18**, 1550 (2002)
79. Nguyen, T.X., Bhatia, S.K.: J. Phys. Chem. B **108**, 14032 (2004)
80. Ustinov, E.A., Do, D.D., Fenelonov, V.B.: Carbon N. Y. **44**, 653 (2006)
81. Ravikovitch, P.I., Neimark, A.V.: Langmuir **22**, 11171 (2006)
82. Neimark, A.V., Lin, Y., Ravikovitch, P.I., Thommes, M.: Carbon N. Y. **47**, 1617 (2009)
83. Jagiello, J., Olivier, J.P.: J. Phys. Chem. C **113**, 19382 (2009)
84. Jagiello, J., Kenvin, J., Olivier, J.P., Lupini, A.R., Contescu, C.I.: Adsorpt. Sci. Technol. **29**, 769 (2011)
85. Jagiello, J., Olivier, J.P.: Carbon N. Y. **55**, 70 (2013)
86. Röcken, P., Somoza, A., Tarazona, P., Findenegg, G.: J. Chem. Phys. **108**, 8689 (1998)
87. Huerta, A., Pizio, O., Bryk, P., Sokolowski, S.: Mol. Phys. **98**, 1859 (2000)
88. Jagiello, J., Jaroniec, M.: J. Colloid Interface Sci. **532**, 588 (2018)
89. Jagiello, J., Kyotani, T., Nishihara, H.: Carbon N. Y. **169**, 205 (2020)
90. Jagiello, J., Olivier, J.P.: Adsorption **19**, 777 (2013)
91. Puziy, A.M., Poddubnaya, O.I., Gawdzik, B., Sobiesiak, M.: Adsorption **22**, 459 (2016)
92. Kruk, M., Jaroniec, M., Gadkaree, K.P.: J. Colloid Interface Sci. **192**, 250 (1997)
93. Miyasaka, K., Neimark, A.V., Terasaki, O.: J. Phys. Chem. C **113**, 791 (2009)
94. Kupgan, G., Liyana-Arachchi, T.P., Colina, C.M.: Langmuir **33**, 11138 (2017)
95. Hansen, P.C., O'Leary, D.P.: SIAM J. Sci. Comput. **14**, 1487 (1993)
96. Thommes, M., Smarsly, B., Groenewolt, M., Ravikovitch, P.I., Neimark, A.V.: Langmuir **22**, 756 (2006)
97. Gor, G.Y., Thommes, M., Cychosz, K.A., Neimark, A.V.: Carbon N. Y. **50**, 1583 (2012)
98. Cychosz, K.A., Guo, X., Fan, W., Cimino, R., Gor, G.Y., Tsapatsis, M., Neimark, A.V., Thommes, M.: Langmuir **28**, 12647 (2012)
99. Lucena, S.M., Oliveira, J.C., Gonçalves, D.V., Silvino, P.F.: Carbon N. Y. **119**, 378 (2017)
100. Lucena, S.M., Paiva, C.A.S., Silvino, P.F., Azevedo, D.C., Cavalcante, C.L.: Carbon N. Y. **48**, 2554 (2010)
101. Rodríguez-Reinoso, F., López-González, J.d.D., Berenguer, C.: Carbon N. Y. **22**, 13 (1984)
102. Jagiello, J., Ania, C., Parra, J.B., Cook, C.: Carbon N. Y. **91**, 330 (2015)
103. Jagiello, J., Kenvin, J., Celzard, A., Fierro, V.: Carbon N. Y. **144**, 206 (2019)
104. Jagiello, J., Kenvin, J., Ania, C.O., Parra, J.B., Celzard, A., Fierro, V.: Carbon N. Y. **160**, 164 (2020)
105. Frenkel, D., Smit, B.: Understanding Molecular Simulation: From Algorithms to Applications, 2nd edn. Academic Press, San Diego (2002)
106. Kowalczyk, P., Gauden, P.A., Furmaniak, S., Terzyk, A.P., Wiśniewski, M., Ilnicka, A., Łukaszewicz, J., Burian, A., Włoch, J., Neimark, A.V.: Carbon N. Y. **111**, 358 (2017)
107. Alexandre de Oliveira, J., Soares Maia, D., Toso, J., Lopez, R., Azevedo, D., Zgrablich, G.: Colloids Surf., A Physicochem. Eng. Asp. **437**, 69 (2013)
108. de Oliveira, J.C.A., López, R.H., Toso, J.P., Lucena, S.M.P., Cavalcante, C.L., Azevedo, D.C.S., Zgrablich, G.: Adsorption **17**, 845 (2011)

109. Ravikovitch, P.I., Vishnyakov, A., Russo, R., Neimark, A.V.: Langmuir **16**, 2311 (2000)
110. Sermoud, V.M., Barbosa, G.D., Barreto, A.G., Tavares, F.W.: Fluid Phase Equilib. **521**, 112700 (2020)
111. Langmuir, I.: J. Am. Chem. Soc. **40**, 1361 (1918)
112. Sips, R.: J. Chem. Phys. **16**, 490 (1948)
113. Do, D.D.: Adsorption Analysis: Equilibria and Kinetics. Published by Imperial College Press and Distributed by World Scientific Publishing Co. (1998)
114. Brunauer, S., Emmett, P.H., Teller, E.: J. Am. Chem. Soc. **60**, 309 (1938)
115. Hill, T.L.: J. Chem. Phys. **14**, 263 (1946)
116. Keii, T.: J. Chem. Phys. **22**, 1617 (1954)
117. Rouquerol, J., Llewellyn, P., Rouquerol, F.: Stud. Surf. Sci. Catal., 49–56 (2007)
118. Llewellyn, P., Maurin, G., Rouquerol, J.: Adsorption by Powders Porous Solids, pp. 565–610. Elsevier (2014)
119. Kaneko, K., Ishii, C., Ruike, M., Kuwabara, H.: Carbon N. Y. **30**, 1075 (1992)
120. Walton, K.S., Snurr, R.Q.: J. Am. Chem. Soc. **129**, 8552 (2007)
121. Gómez-Gualdrón, D.A., Moghadam, P.Z., Hupp, J.T., Farha, O.K., Snurr, R.Q.: J. Am. Chem. Soc. **138**, 215 (2016)
122. Sinha, P., Datar, A., Jeong, C., Deng, X., Chung, Y.G., Lin, L.-C.: J. Phys. Chem. C **123**, 20195 (2019)
123. Adolphs, J., Setzer, M.J.: J. Colloid Interface Sci. **180**, 70 (1996)
124. Adolphs, J.: Appl. Surf. Sci. **253**, 5645 (2007)
125. de Lange, M.F., Lin, L.-C., Gascon, J., Vlugt, T.J.H., Kapteijn, F.: Langmuir **32**, 12664 (2016)
126. Brunauer, S., Emmett, P.H.: J. Am. Chem. Soc. **59**, 2682 (1937)
127. Brunauer, S.: The Adsorption of Gases and Vapours, vol. 1. Physical Adsorption. Oxford University Press (1943)
128. Rouquerol, J., Partyka, S., Rouquerol, F.: J. Chem. Soc. Faraday Trans. 1 Phys. Chem. Condens. Phases **73**, 306 (1977)
129. Gardner, L., Kruk, M., Jaroniec, M.: J. Phys. Chem. B **105**, 12516 (2001)
130. Lowell, S., Shields, J., Charalambous, G., Manzione, J.: J. Colloid Interface Sci. **86**, 191 (1982)
131. McClellan, A., Harnsberger, H.: J. Colloid Interface Sci. **23**, 577 (1967)
132. Ambroz, F., Macdonald, T.J., Martis, V., Parkin, I.P.: Small Methods **2**, 1800173 (2018)
133. Géron, A.: Hands-on Machine Learning with Scikit-Learn, Keras, and TensorFlow: Concepts, Tools, and Techniques to Build Intelligent Systems, 2nd Editio. O'Reilly Media, Inc. (2019)
134. Datar, A., Chung, Y.G., Lin, L.-C.: J. Phys. Chem. Lett. **11**, 5412 (2020)
135. Tibshirani, R., Stat, J.R.: Soc. Ser. B **58**, 267 (1996)
136. Alqahtani, N., Alzubaidi, F., Armstrong, R.T., Swietojanski, P., Mostaghimi, P.: J. Pet. Sci. Eng. **184**, 106514 (2020)
137. Krizhevsky, A., Sutskever, I., Hinton, G.E.: Advances in Neural Information Processing Systems, vol. 25, pp. 1097–1105 (Pereira, F., Burges, C.J.C., Bottou, L., Weinberger, K.Q., eds.). Curran Associates, Inc. (2012)
138. Shi, K., Santiso, E.E., Gubbins, K.E.: Langmuir **35**, 5975 (2019)
139. Shi, K., Santiso, E.E., Gubbins, K.E.: Langmuir **36**, 1822 (2020)
140. Forte, E., Haslam, A.J., Jackson, G., Müller, E.A.: Phys. Chem. Chem. Phys. **16**, 19165 (2014)
141. Ravipati, S., Galindo, A., Jackson, G., Haslam, A.J.: Phys. Chem. Chem. Phys. **21**, 25558 (2019)
142. Balzer, C., Waag, A.M., Gehret, S., Reichenauer, G., Putz, F., Hüsing, N., Paris, O., Bernstein, N., Gor, G.Y., Neimark, A.V.: Langmuir **33**, 5592 (2017)